

Supporting Information (SI)

for

**Accelerated Fe²⁺ Regeneration in Effective Electro-Fenton Process by Boosting
Internal Electron Transfer to Nitrogen-Conjugated Fe(III)-Complex**

Mingyue Liu^a, Zhiyuan Feng^a, Xinmiao Luan^b, Wenhai Chu^b, Hongying Zhao^{a*},
Guohua Zhao^a

^a School of Chemical Science and Engineering, Shanghai Key Lab of Chemical Assessment and Sustainability, Key Laboratory of Yangtze River Water Environment, Tongji University, Siping Road 1239, Shanghai 200092, P. R. China

^b State Key Laboratory of Pollution Control and Resources Reuse, College of Environmental Science and Engineering, Tongji University, Siping Road 1239, Shanghai 200092, P. R. China

* Corresponding authors Tel.: +86-(0)21-65988570-8436;

Fax: +86-(0)21-65982287

* E-mail addresses: hyzhao@tongji.edu.cn

CONTENT

Supplementary Methods	SError! Bookmark not defined.
Table S1. Intermediate products in DMP degradation process determined by gas chromatography-time-of-flight mass spectrometry (GC-MS) analysis.	S10
Table S2. Fe ²⁺ regeneration efficiency of reported techniques.	S11
Table S3. Atom ratio of Fe(II) and Fe(III) of NDCA cathode.....	S12
Table S4. The distribution of pyridinic-N, pyrrolic-N, graphitic-N, pyridinic-N ⁺ -O ⁻ and Fe-N _x in fresh and used NDCA cathode.....	S13
Table S5. Chemical and physical properties of NDCA, NDCA-C1 and NACA-C2 including BET specific area, resistance and electrochemical impedance.....	S14
Table S6. The distribution of pyridinic-N, pyrrolic-N, graphitic-N and pyridinic-N ⁺ -O ⁻ of NDCA, NDCA-C1, NDCA-C2, respectively.	S15
Table S7. Parameters obtained from fitting the Mössbauer spectra of used NDCA taken at 298 K and Fe-N reported in literature: isomer shift (IS, mm s ⁻¹), quadrupole splitting (QS, mm s ⁻¹) and line width (LW, mm s ⁻¹) of D1.	S16
Table S8. Comparison on DMP degradation efficiency, stability and energy consumption of different advanced oxidation processes	S17
Figure S1. SEM image of NDCA (a) before and (b) after EF process.....	S19
Figure S2. TEM images of NDCA at different magnifications with scale bar of (a) 20 nm and (b) 2 nm.	S20
Figure S3. (a) EDX pattern of NDCA cathode and elementary mapping of (b) carbon, (c) nitrogen and (d) oxygen.....	S22

Figure S4. Raman spectrum of NDCA, NDCA-C1 and NDCA-C2 cathodes.	S23
Figure S5. ESR spectrums of EF system using NDCA cathode under different current of 10 mA, 20 mA and 30 mA.	S24
Figure S6. Linear sweep voltammetry (LSV) curve of (a) ORR and (b) Fe^{3+} reduction with NDCA acted as working electrode in O_2 atmosphere with 0.01 M Na_2SO_4	S25
Figure S7. The bias potential of NDCA electrode under different current of 10 mA (1.67 mA cm^{-2}), 20 mA (3.33 mA cm^{-2}) and 30 mA (5 mA cm^{-2}), respectively.	S27
Figure S8. ESR spectrums of EF system using NDCA cathode with different Fe^{2+} dosage of 0.2 mM, 0.5 mM, 1.0 mM, 2.0 mM and 5.0 mM.	S28
Figure S10. DMP removal efficiency in ES process with NDCA cathode.	S30
Figure S11. The degradation mechanism of DMP in $\cdot\text{OH}$ -mediated process.	S31
Figure S12. Evolution of the inhibition of marine bacterial luminescence after 5 and 15 min of exposure with a sample taken after different EF treatment duration for DMP degradation.	S33
Figure S13. The ESR spectrums of Fe^{2+} /NDCA-EF system at various time of 5, 30, 60, 120, 180 and 240 min.	S34
Figure S14. The concentration of total dissolved iron in Fe^{2+} /NDCA-EF system.	S35
Figure S15. The pH values during the whole EF reaction from 0 to 270 min.	S36
Figure S16. The Fe(III) distribution at various reaction time from 0 to 270 min.	S37
Figure S17. The distribution of Fe^{3+} , Fe(OH)_2^+ , FeSO_4^+ and FeOH^{2+} species.	S38
Figure S18. The Nyquist curves of CA and NDCA with the frequency from 0.1 Hz to 10000 Hz.	S39

Figure S19. The Fe 2p spectrum of NDCA cathode after EF reaction for 40 min....	S40
Figure S20. The N 1s spectrum of (a) NDCA-C1 and (b) NDCA-C2. (c) H ₂ O ₂ yield by NDCA, NDCA-C1 and NDCA-C2 after 60 min with current of 20 mA. (d) The concentration of Fe ²⁺ during EF reaction with same amount of 60 ppm H ₂ O ₂ including the electro-generated H ₂ O ₂ via cathode and externally supplied H ₂ O ₂	S41
Figure S21 Fe ²⁺ regeneration efficiency with different cathode including NDCA, NDCA-C1 and NDCA-C2 with different atom ratio of pyrrolic-N.....	S42
Figure S22. The Fe(II) distribution at various pH values, calculated based on the database in Visual MINTEQ.	S43
Figure S23. The concentration of Fe ²⁺ in EF process with different cathodes including NDCA, CC, CF and pure CA.....	S44

1. Chemicals

The solvents and reagents used in this system were directly applied without additional purification. Sodium sulfate (Na_2SO_4 , AR, 99.0%, CAS: 7757-82-6), sodium fluoride (NaF , 98.0%, CAS: 7681-49-4), sodium carbonate (Na_2CO_3 , AR, $\geq 99.5\%$, CAS: 497-19-8), potassium ferricyanide ($\text{K}_3[\text{Fe}(\text{CN})_6]$, AR, $\geq 99.5\%$, CAS: 13746-66-2), potassium ferrocyanide ($\text{K}_4\text{Fe}(\text{CN})_6 \cdot 3\text{H}_2\text{O}$, AR, 99.0%, CAS: 14459-95-1), acetone (AR, $\geq 99.5\%$, CAS: 67-64-1), ethanol (AR, 99.7%, CAS: 64-17-5), hydroxylamine hydrochloride (AR, 98.5%, CAS: 5470-11-1), ammonium acetate ($\text{CH}_3\text{COO}(\text{NH}_4)_2$, AR, 98.0%, CAS: 631-61-8), titanium oxysulfate (TiOSO_4 , 93.0%, CAS: 123334-00-9) and resorcinol (AR, $\geq 99.0\%$, CAS: 108-46-3) were purchased from Sinopharm Chemical Reagent Co., Ltd. 1,10-Phenanthroline (AR, 97.0%, CAS: 3829-86-5) and 2,4-dinitrophenylhydrazine (98.0%, CAS: 119-26-6) were purchased from Adamas Reagent Co., Ltd. Sulfamethoxazole (SMX, AR, 98.0%, CAS: 723-46-6), bisphenol A (BPA, $>99.0\%$, CAS: 80-05-7), 3-chlorophenol (3-CP, 98.0%, CAS: 108-43-0), dimethyl phthalate (DMP, AR, $>99.0\%$, CAS: 131-11-3), ferrous sulfate heptahydrate ($\text{FeSO}_4 \cdot \text{H}_2\text{O}$, AR, $\geq 99.0\%$, CAS: 7782-63-0), 5,5-dimethyl-1-pyrrolin-N-oxide (DMPO, RG, $\geq 98.0\%$, CAS: 1073-23-0), and dimethyl sulfoxide (DMSO, AR, $\geq 99.8\%$, CAS: 67-68-5) were purchased from Sigma-Aladdin Bio-Chem Technology Co., Ltd. Acetonitrile (GC, $\geq 99.8\%$, CAS: 75-05-8) were purchased from Germany Merck KGaA. Oxygen (O_2 , 99.998%, CAS: 7782-44-7), nitrogen (N_2 , 99.998%, CAS: 7727-37-9), and carbon dioxide (CO_2 , 99.998%, CAS: 124-38-9) were purchased from Shanghai Qingkuan Chemical Co., Ltd. A Milli-Q purification system supplies all the deionized

water with resistivity of 18.2 M Ω ·cm.

2. Characterization methods

The specific surface area of NDCA cathodes were calculated by N₂ adsorption data with relative pressure of 0.05-0.2 using the Brunauer-Emmett-Teller (BET) model by Micromeritics ASAP 3020 surface area analyzer. Water contact angle reflects the hydrophobicity of different NDCA cathodes. To obtain the morphology information of NDCA gels, the scanning electron microscopy (SEM) and energy dispersive X-ray spectroscopy (EDX) were conducted by Hitachi-S4800. Transmission electron microscopy (TEM) images were captured on a JEM 2100 operated at 200 kV. The defects of NDCA cathodes were reflected by Raman spectra, which was determined by Raman spectrometer with argon ion as laser resource at 514.5 nm. X-ray photoelectron spectroscopy (XPS) was conducted by Kratos AXIS-HS with a focused monochromatic Al K α X-ray radiation (150 W, 15 kV, 10 mA), taking the binding energy of C1s peak at 284.6 eV as the reference for calibration. What's more, the X-ray absorption fine structure (XAFS) spectroscopy data were obtained at BL11B beamline in Shanghai Synchrotron Radiation Facility (SSRF) in transmission model to obtain the deep information of Fe K edge.

3. Electrochemical procedures

Cyclic voltammetry (CV) electrochemical experiments were conducted to reveal the interaction between cathode and iron species. 10 mg NDCA and pure CA were put into 1.5 mL water respectively, then 750 μ L of Nafion and 250 μ L of alcohol was added into the mixed solution. After ultrasound treatment for 1 h at 0 $^{\circ}$ C, 25 μ L of the obtained

solution were withdrawn and drop to the surface of clean glassy carbon electrode. Then CV experiments were performed with following parameters: initial E of -0.3 V, high E of 0.7 V and scan rate of 0.01 V s⁻¹. The electrolyte was 5 mM K₃[Fe(CN)₆].

4. Concertation of H₂O₂

The yield of H₂O₂ was measured through spectrophotometric method since titanium oxysulfate reacted with H₂O₂ and the corresponding product had the maximum adsorption wavelength of 406 nm. Thus, it could be detected by UV-Vis spectrophotometer (Agilent 8453, Agilent Corporation, U.S.).

5. Distribution of Fe species

The amounts of iron species including total dissolved iron and dissolved Fe²⁺ were also determined by a spectrophotometric way since 1,10-phenanthroline could adduct with Fe²⁺ and the complex had a maximum adsorption wavelength at 510 nm. More specifically, to determine the dissolved ferrous ion, 0.5 mL acetic acid-ammonium acetate buffer, 0.2 mL 1,10-phenanthroline (0.15 w.t. %) and 3.3 mL deionized water were mixed followed by adding 1 mL sample obtained at specific intervals. As for calculating the amount of total dissolved iron, 0.5 mL acetic acid-ammonium acetate buffer, 0.2 mL 1,10-phenanthroline, 0.2 mL hydroxylamine hydrochloride (10 w.t.%) and 3.1 mL deionized water were mixed followed by adding 1 mL sample. The mixture was then taken to be measured by UV-Vis spectrophotometer to measuring the concentration of ferrous ion and total dissolved iron. Besides, the speciation of ferric ion at different time was calculated by Visual MINTEQ and its database.

6. Analytical process for organic pollutants

The concentration of pollutants was determined by high-performance liquid chromatography (HPLC-UV, Thermofisher, USA) equipped with a reverse ZORBA X Eclipse Plus C18 column (5 μm particle size, 4.6 mm \times 250 mm). The mobile phases and detection UV wavelengths were set as: methanol/water (60:40, V/V) with $\lambda=230$ nm at 25 $^{\circ}\text{C}$ for DMP, methanol/water (70:30, V/V) with $\lambda=273$ nm at 30 $^{\circ}\text{C}$ for 3-CP, methanol/water (40:60, V/V) with $\lambda=300$ nm at 30 $^{\circ}\text{C}$ for SMX and methanol/water (70:30, V/V) with $\lambda=225$ nm at 30 $^{\circ}\text{C}$ for BPA. The flow rate of mobile phase was all set as 1 mL min⁻¹. The total organic carbon (TOC) was analyzed through a TOC analyzer (multi N/C 3100 TOC/TN analyzer, Analytikjena, Germany).

7. Determination of standard deviation

Standard deviation (σ) was calculated based on equation S1:

$$\sigma = \sqrt{\frac{\sum_{i=1}^n (x_i - \mu)^2}{n}} \quad (\text{S1})$$

where σ is standard deviation (s. d.), x_i is the actual measured value, μ is the mean value, n refers to the number of repeated experiments, and the value of n is 3 in this work.

8. Toxicity tests

The toxicity of dimethyl phthalate (DMP) and its intermediate by-products produced during its degradation was assessed by measuring the effect on the luminescence of marine bacterial, as the emitted luminescence of bacterium was related to cell activity.^{1,2} Bacterial luminescence was measured using a Microtox[®] Model 500 Analyzer (Modern Water Inc.; United Kingdom) with the software MicrotoxOmni[®].

The bacteria used in this method was the strain *Vibrio fischeri* NRRL B-11177.

Ten concentration series in three parallels and 10 controls were arranged in a microplate and the test was repeated three times. The relative light units (LU) of *Vibrio fischeri* were determined after 5 min and 15 min exposure to the toxicant. The toxicity of DMP and its intermediates is expressed as the inhibition rate, which is calculated by equation S2:

$$I (\%) = (1 - \frac{LU(t)}{LU(0)}) \times 100 \quad (S2)$$

where LU(t) is the intensity of luminescence emitted by bacteria after a t = 5 min or t = 15 min of contact with the toxicant, LU(0) is the initial intensity of luminescence emitted by bacteria before the addition of sample.

However, time and the action of environmental conditions also decrease the luminescence. Errors compensate need to be considered due to these factors by taking into account the variability of the luminescence R(t) in a control solution as corrected term, which is calculated by equation S3:

$$R(t) = \frac{LU(t)}{LU0(0)} \quad (S3)$$

where LU0(0) is the initial intensity of luminescence emitted by bacteria before the addition of the control solution (Milli Q water and NaCl).

Then the corrected inhibition rate (Ic) intrinsically attributable to the sample toxicity is calculated using equation S4:

$$Ic (\%) = (1 - \frac{LU(t)}{R(t) \times LU(0)}) \times 100 \quad (S4)$$

Table S1. Intermediate products in DMP degradation process determined by gas chromatography-time-of-flight mass spectrometry (GC-MS) analysis.

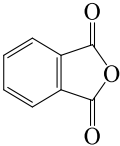
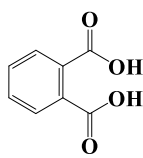
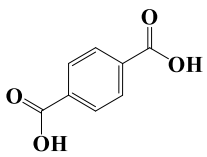
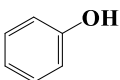
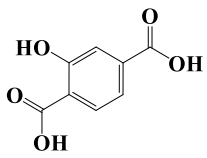
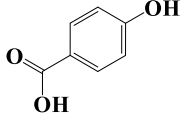
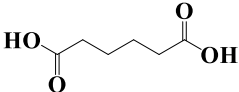
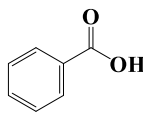
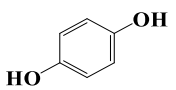
Intermediates	Formula	Molecular structure	m/z
o-Phthalic anhydride (PAH)	C ₈ H ₄ O ₃		147
Phthalic acid (PA)	C ₈ H ₆ O ₄		166
p-Phthalic acid (pPA)	C ₈ H ₆ O ₄		223
Phenol (PH)	C ₆ H ₆ O		130
2-hydroxyterephthalic acid (HTA)	C ₈ H ₆ O ₅		241
4-hydroxybenzoic acid (HBA)	C ₇ H ₆ O ₃		152
Terephthalic acid (TA)	C ₆ H ₁₀ O ₂		121
Benzoic acid (BA)	C ₇ H ₆ O ₂		44
1,4-benzenediol (BD)	C ₆ H ₆ O ₂		109

Table S2. Fe²⁺ regeneration efficiency of reported techniques with different materials.

Methods	Other parameters	Initial Concentration of Fe ²⁺ (ppm)	Time for equilibrium status (min)	Fe ²⁺ regeneration (%)	Ref.
Fenton-AA	0.4 mM H ₂ O ₂ , pH 3.0	28×10 ⁻³	120	40.0%	3
Fenton-WS ₂	0.1 mM H ₂ O ₂ , pH 3.8	40	30	30.0%	4
EF-double potential	-0.5V 15s + -0.1V 15s, pH 3.0	28	60	24.0%	5
PF-Vis-γCeO ₂ /Fh	5W light, 50 mM H ₂ O ₂ , pH 4.0	56	60	50.0%	6
Fe ²⁺ /NDCA-EF	3.3 mA cm ⁻² , pH 3.0	56	40	56.3%	this work

As shown in Table S2, Fe²⁺/NDCA-EF process possessed the highest Fe²⁺ regeneration efficiency of 56.3%, which is 1.08~2.25 times higher than other systems including AA, WS₂, EF-double potential and PE systems. Additionally, the concentration of Fe²⁺ in Fe²⁺/NDCA-EF process reached to equilibrium in 40 min, which is shorter than that of AA, EF-double potential and PF processes in 120 min, 60 min and 60 min, respectively. Thus, it is reasonable to indicate that the nitrogen-doped carbon aerogel can be acted as a promising reducing agent in traditional EF process for the regeneration of Fe²⁺ without using foreign reagents.

Table S3. Atom ratio of Fe(II) and Fe(III) of NDCA cathode.

Fe atom	NDCA-40min	NDCA-270min
Fe(II)	39%	47%
Fe(III)	61%	53%

Table S4. The distribution of pyridinic-N, pyrrolic-N, graphitic-N, pyridinic-N⁺-O⁻ and Fe-N_x in fresh and used NDCA cathode.

N atom	Fresh NDCA	Used NDCA
Pyridinic-N	13%	3%
Pyrrolic-N	40%	28%
Graphitic-N	35%	9%
Pyridinic-N⁺-O⁻	12%	24%
Fe-N_x	--	38

Table S5. Chemical and physical properties of NDCA, NDCA-C1 and NDCA-C2 including BET specific area, resistance and electrochemical impedance.

Sample	Temp. (°C)	Specific area (m ² g ⁻¹)	Resistance (Ω cm ⁻¹)	Impedance (Ω)
NDCA	750	578	9	16
NDCA-C1	850	607	7	14
NDCA-C2	950	639	17	31

As shown in Table S5, the specific area of nitrogen-doped carbon aerogel increased from 578 m² g⁻¹ to 639 m² g⁻¹ when increasing the calcination temperature from 750 to 850 °C. At higher calcination temperature, carbon matrix would be more active to react with CO₂ and then cause the emission of CO, leading to high BET surface area. The value of physical resistance was 9, 7, and 17 Ω cm⁻¹ as well as the electrochemical impedance was 16, 14, and 31 Ω for NDCA, NDCA-C1 and NDCA-C2, respectively. The observation indicates that integrated carbon aerogel electrodes possess good conductivity after the introduction of N dopants.

Table S6. The distribution of pyridinic-N, pyrrolic-N, graphitic-N and pyridinic-N⁺-O⁻ of NDCA, NDCA-C1, NDCA-C2, respectively.

Sample	Temp. (°C)	Pyrrolic-N (at%)	Graphitic-N (at%)	Pyridinic-N (at%)	Pyridinic-N⁺-O⁻ (at%)
NDCA	750	40%	35%	13%	12%
NDCA-C1	850	32%	43%	12%	15%
NDCA-C2	950	10%	51%	10%	29%

Table S7. Parameters obtained from fitting the Mössbauer spectra of used NDCA taken at 298 K and Fe-N reported in literature: isomer shift (IS, mm s⁻¹), quadrupole splitting (QS, mm s⁻¹) and line width (LW, mm s⁻¹) of D1.

Sample	IS mm s⁻¹	QS mm s⁻¹	LW mm s⁻¹
NDCA	0.350 ± 0.003	0.659 ± 0.006	0.473 ± 0.009
Fe-N ⁷	0.356 ± 0.002	0.671 ± 0.003	0.470 ± 0.007

As listed in Table S7, the parameters of D1 obtained from the Mössbauer spectra of used NDCA included isomer shift (IS), quadrupole splitting (QS) and line width (LW). The values of these parameters fitted well with the Fe-N (with Fe-N bond) as reported in literature, confirming the presence of Fe-N bond in NDCA electrode as stated in Figure 4d.

Table S8. Comparison on DMP degradation efficiency, stability and energy consumption of different advanced oxidation processes

Methods	Other parameters	Initial conc. of DMP (ppm)	Removal efficiency (%)	Reaction time (min)	k_{obs} (h ⁻¹)	Stability ^a	SEC (kW·h·g ⁻¹)	Ref.
EO-Ce-doped Ti/PbO₂	25.0 mA cm ⁻² , pH 7.0 0.05 M Na ₂ SO ₄	5.0	95.8%	600	0.29	91.6% after 5 runs	1.20	8
EF-B/N-doped GF	17.6 mA cm ⁻² 0.05 M Na ₂ SO ₄ 0.1 mM Fe ²⁺ , pH 3.0	50.0	100.0%	120	3.84	85.0% after 5 runs	1.12	9
UV/H₂O₂	0.025 mM H ₂ O ₂ UV light 17.1 μW/cm ²	9.7	95.4%	30	4.14	--	1.41	10
PF-Vis/CuO/GCN	0.1 mM H ₂ O ₂ , pH 4.0 light intensity 750 lx	19.4	99.0%	120	0.72	94.0% after 5 runs	0.97	11
SPC+plasma	18 kV 0.12 mM SPC	30.0	97.0%	45	3.90	--	1.08	12
Fe²⁺/NDCA-EF	3.3 mA cm ⁻² 0.05 M Na ₂ SO ₄ 1.0 mM Fe ²⁺ , pH 3.0	10.0	100.0%	50	5.31	100.0% after 5 runs	0.36	This work

a. The stability of different catalysts or cathodes is evaluated by the DMP removal efficiency after five cyclic experiments.

In order to further evaluate the catalytic oxidation performance of $\text{Fe}^{2+}/\text{NDCA}$, the DMP removal in different advanced oxidation processes (AOPs) was assessed, as shown in Table S8. Almost 95.4-100.0% DMP was efficiently removed in the reported AOPs. However, $\text{Fe}^{2+}/\text{NDCA}$ has the k_{obs} of 5.31 h^{-1} , which is 1.2~18.3 times higher than in EO-Ce-doped Ti/PbO_2 (0.29 h^{-1}), EF-B/N-doped GF (3.84 h^{-1}), UV/ H_2O_2 (4.14 h^{-1}), PF-Vis/ CuO/GCN (0.72 h^{-1}), and SPC+plasma (3.90 h^{-1}), respectively. Moreover, the specific energy consumption (SEC) of complete DMP removal in $\text{Fe}^{2+}/\text{NDCA}$ -EF process was $0.36 \text{ kW}\cdot\text{h}\cdot\text{g}^{-1}$, which only accounted for 25.5~37.0% in other traditional AOPs. The stability of the catalysts and electrodes was revealed by the DMP removal efficiency after five runs. In $\text{Fe}^{2+}/\text{NDCA}$ -EF system, DMP degradation efficiency remained at 100.0%, while the maximum removal of DMP in other AOPs decreased by 4.2~15.0%. These advantages endow NDCA cathode with great prospect in EF process for practical applications.

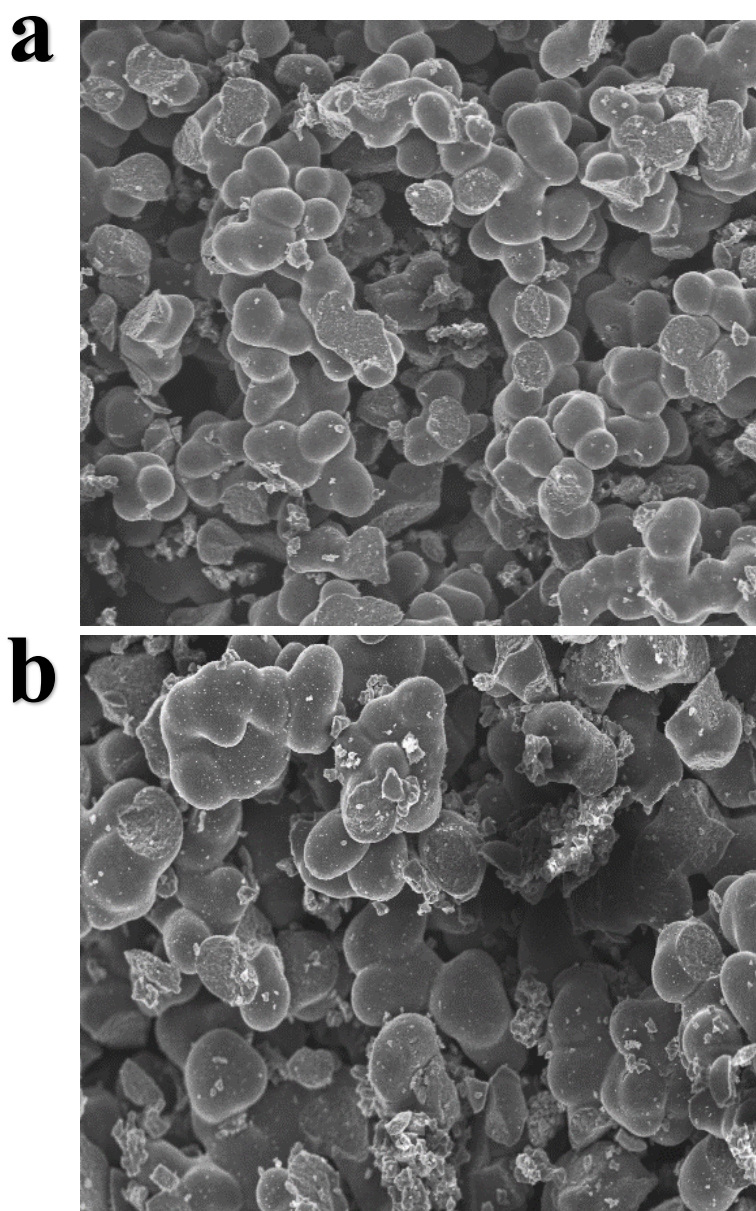


Figure S1. SEM image of NDCA (a) before and (b) after EF process.

As shown in Figure S1a, NDCA material has a three-dimensional mesh structure composed of microsphere connected with each other and the surface of microsphere was smooth. The morphology of NDCA after EF process didn't exhibit obvious difference compared with fresh NDCA, revealing the high stability of NDCA cathode.

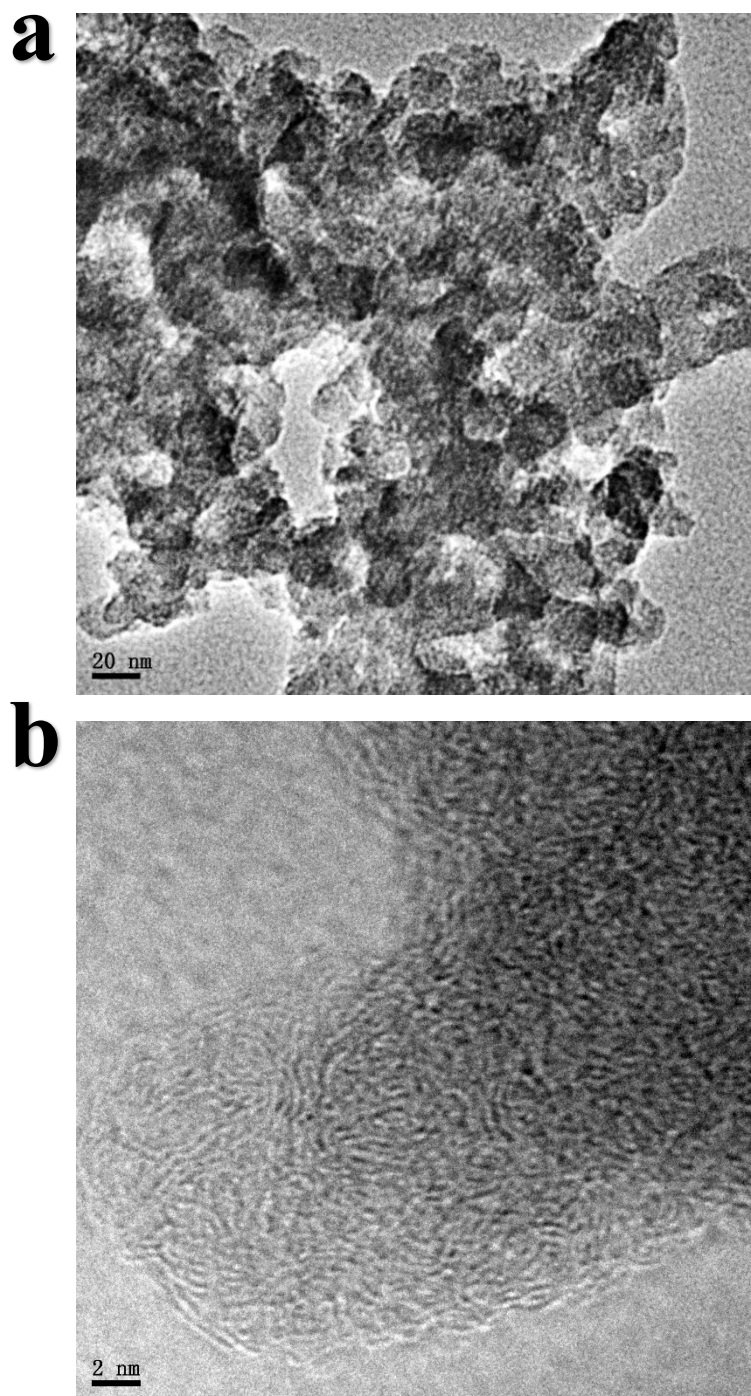


Figure S2. TEM images of NDCA at different magnifications with scale bar of (a) 20 nm and (b) 2 nm.

The TEM images of NDCA cathode at various magnifications was shown in Figure S2. It can be clearly seen that the NDCA material was composed by stacks of three dimensional microspheres, which is consistent with the SEM image. Besides, the

carbon matrix exists in the form of amorphous carbon with sufficient defects, consistent with the Raman spectrum as shown in Figure S4.

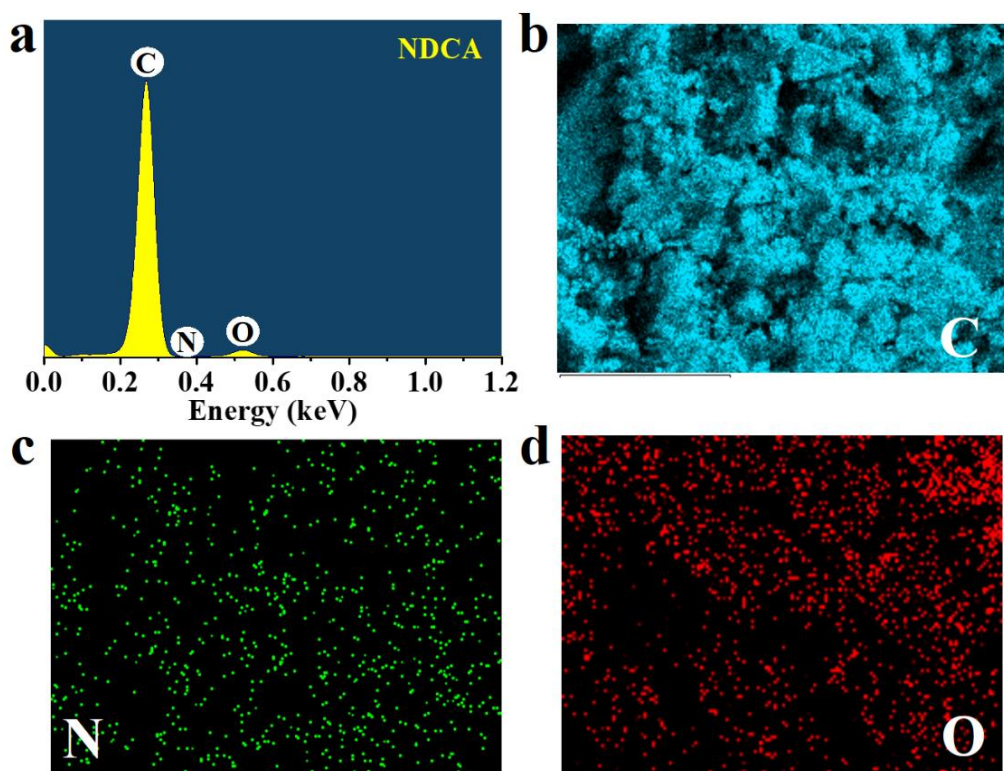


Figure S3. (a) EDX pattern of NDCA cathode and elementary mapping of (b) carbon, (c) nitrogen and (d) oxygen.

As shown in Figure S3a, the presence of surface nitrogen on NDCA electrode was confirmed by EDX analysis, confirming the successful doping of N. Besides, the NDCA contains several kinds of elements including C, N, O with distribution of 93.76 wt%, 0.55 wt%, and 5.69 wt%. The element maps of N (green) are uniformly distributed on the C (blue) together with a coverage of O (red) on the surface of NDCA electrode.

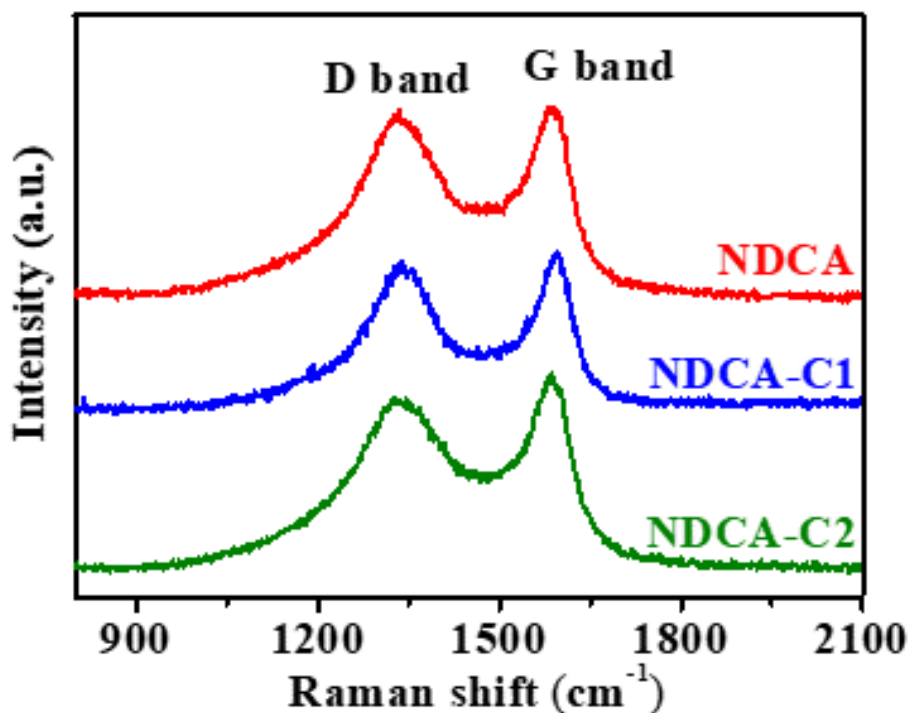


Figure S4. Raman spectrum of NDCA, NDCA-C1 and NDCA-C2 cathodes.

The defective nature of NDCA, NDCA-C1 and NDCA-C2 cathodes were investigated by Raman spectra as shown in Figure S4. All the Raman spectra presented two major bands, which are denoted as D band (1335 cm^{-1}) and G band (1580 cm^{-1}), designated to the disordered and graphitic carbon phases, respectively. The ratio of the integrated intensities of the D to G band (I_D/I_G) was used to assess the defects present in graphitic structures. the I_D/I_G values of NDCA, NDCA-C1 and NDCA-C2 were 0.92, 0.89 and 0.83, respectively, revealing that the defects in graphitic carbon matrix decreased at higher calcination temperature. Higher amount of defects led to more production of H_2O_2 ,¹³ which was consistent with the result in Figure S19c that NDCA had the highest H_2O_2 yield compared with NDCA-C1 and NDCA-C2.

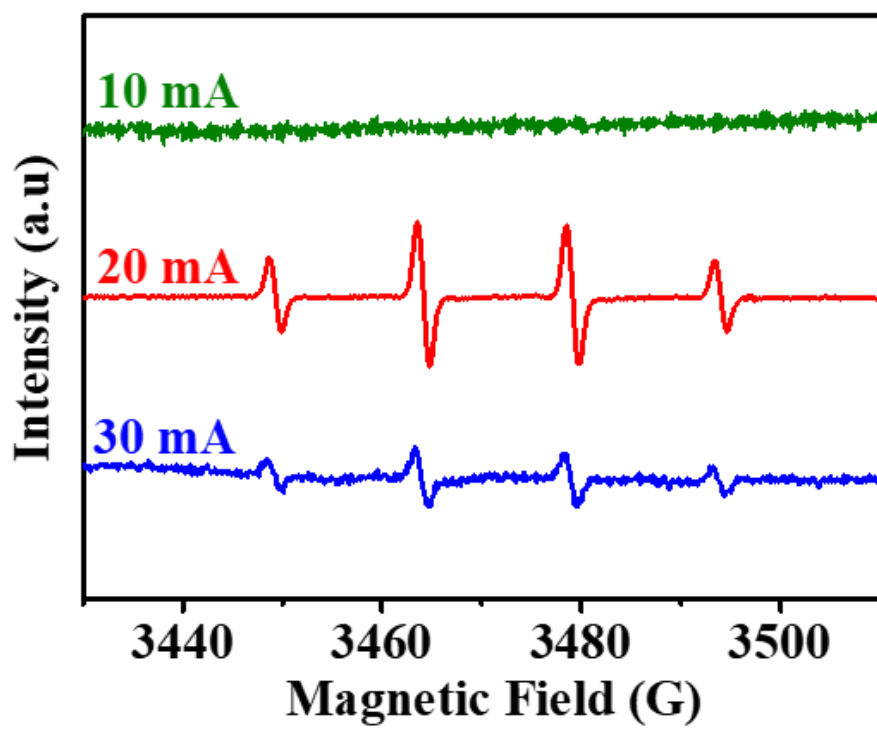


Figure S5. ESR spectrums of EF system using NDCA cathode under different current of 10 mA, 20 mA and 30 mA.

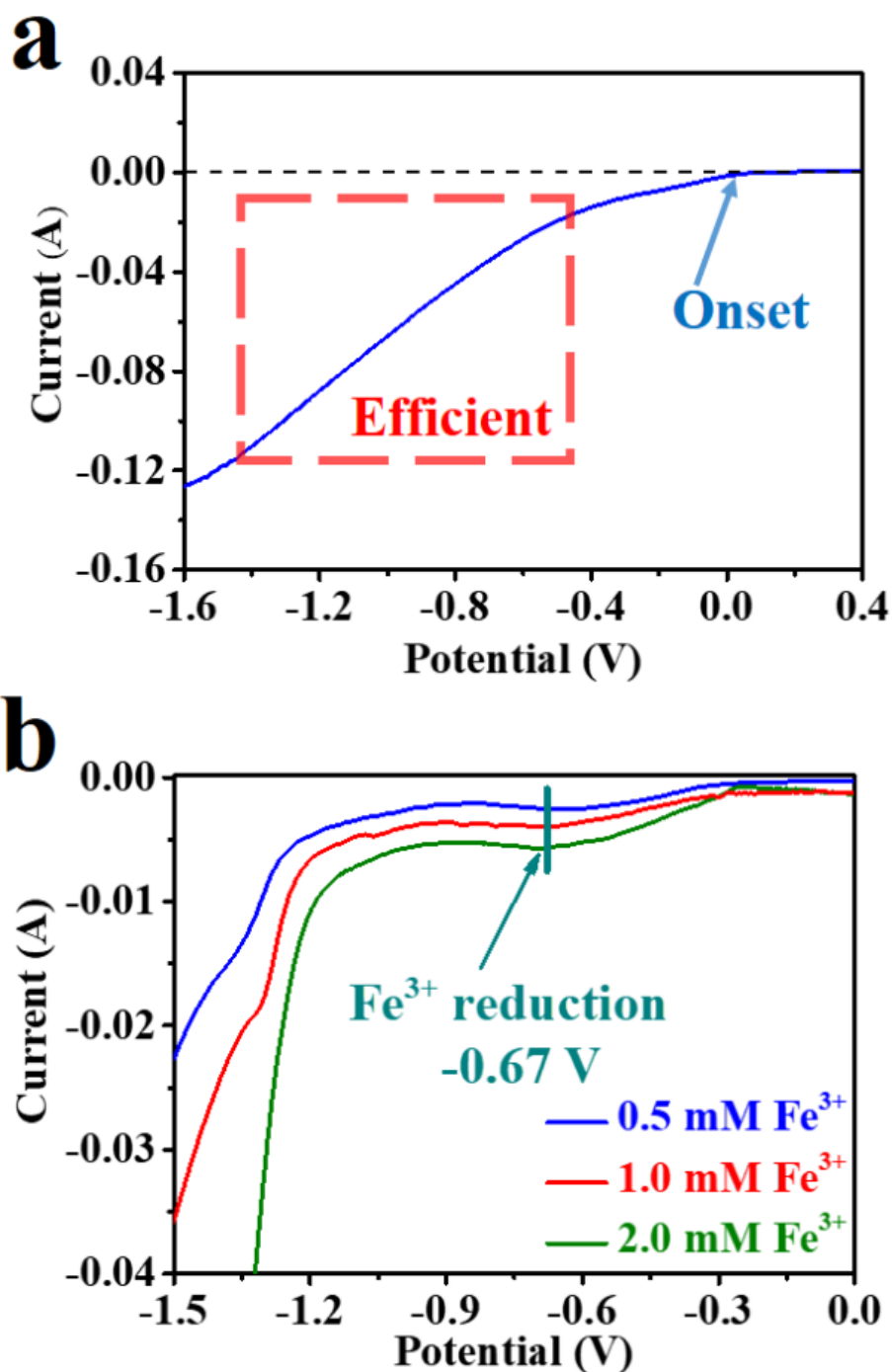


Figure S6. Linear sweep voltammetry (LSV) curve of (a) ORR and (b) Fe^{3+} reduction with NDCA acted as working electrode in O_2 atmosphere with 0.01 M Na_2SO_4 at pH=3.

As shown in Figure S6a, the ORR was initiated at -0.1 V (vs. SCE), while the ORR current increased rapidly when potential negatively shifted to the range of -0.5 ~ -1.4

V (vs. SCE), which is more efficient for H₂O₂ production. Moreover, as shown in Figure S7b, an obvious reduction peak (-0.67 V vs. SCE) was obtained by introducing different dosage of Fe³⁺ (0.5 mM, 1.0 mM and 2.0 mM) into electrolyte. Therefore, the optimal potential in Fe²⁺/NDCA-EF system lies in the range of (-0.67 ~ -1.4 V vs. SCE), which is beneficial for not only ORR reaction but also Fe³⁺ reduction.

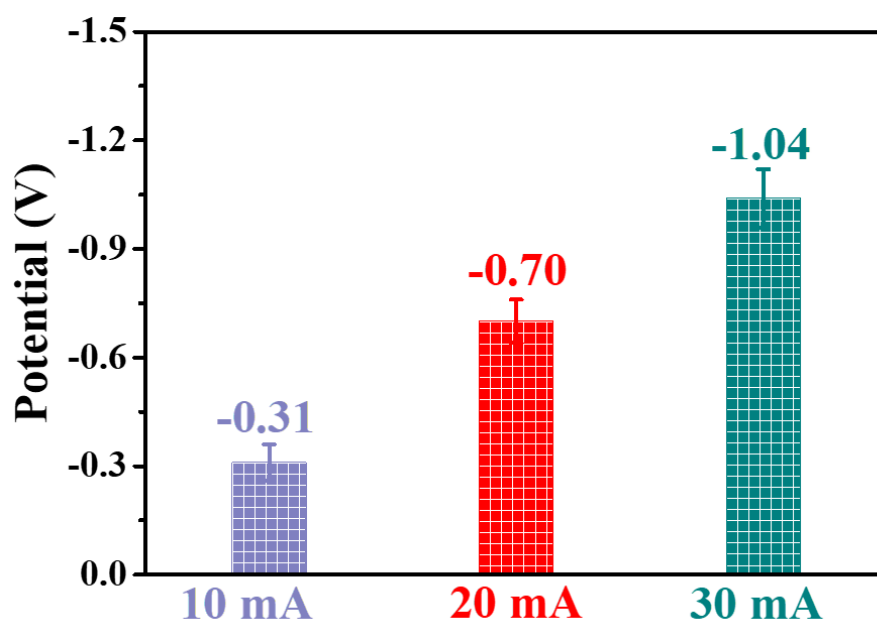


Figure S7. The bias potential of NDCA electrode under different current of 10 mA (1.67 mA cm^{-2}), 20 mA (3.33 mA cm^{-2}) and 30 mA (5 mA cm^{-2}), respectively.

As shown in Figure S5, the bias potential of NDCA electrode at equilibrium state was -0.31, -0.70 and -1.04 V (vs. SCE). According to the optimal potential for ORR ($-0.5 \sim -1.4 \text{ V}$) and Fe^{3+} reduction (-0.68 V), the optimal current should be 20 mA (3.33 mA cm^{-2}) with corresponding potential of -0.70 V, which was benefit for both ORR and Fe^{3+} reduction. When the applied current increased to 30 mA, the bias potential was much higher than the potential for Fe^{3+} reduction potential, which inhibited the Fe^{2+} regeneration and increased the economic cost. Therefore, the applied current was chosen as 20 mA, which not only provided the best potential for efficiently producing H_2O_2 and regenerating Fe^{2+} , but also decreased the cost for actual application in wastewater remediation.

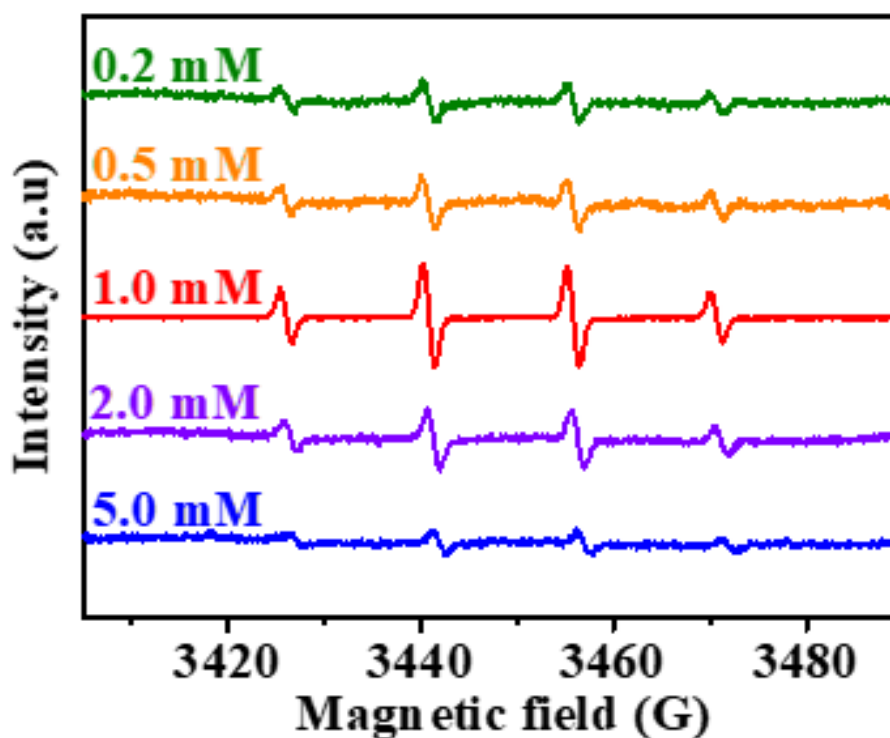


Figure S8. ESR spectrums of EF system using NDCA cathode with different Fe^{2+} dosage of 0.2 mM, 0.5 mM, 1.0 mM, 2.0 mM and 5.0 mM.

The optimal dosage of Fe^{2+} was determined by comparing the ESR signals with different Fe^{2+} concentration of 0.2, 0.5, 1.0, 2.0 and 5.0 mM as shown in Figure S8. When the concentration of Fe^{2+} increased from 0.2 mM to 1.0 mM, the intensity of ESR signal increased rapidly due to more amount of Fenton active sites in EF system. However, as the Fe^{2+} dosage further increased to 5.0 mM, the intensity of ESR signal decreased due to the scavenging of $\cdot\text{OH}$ by extra Fe^{2+} ions¹⁴.

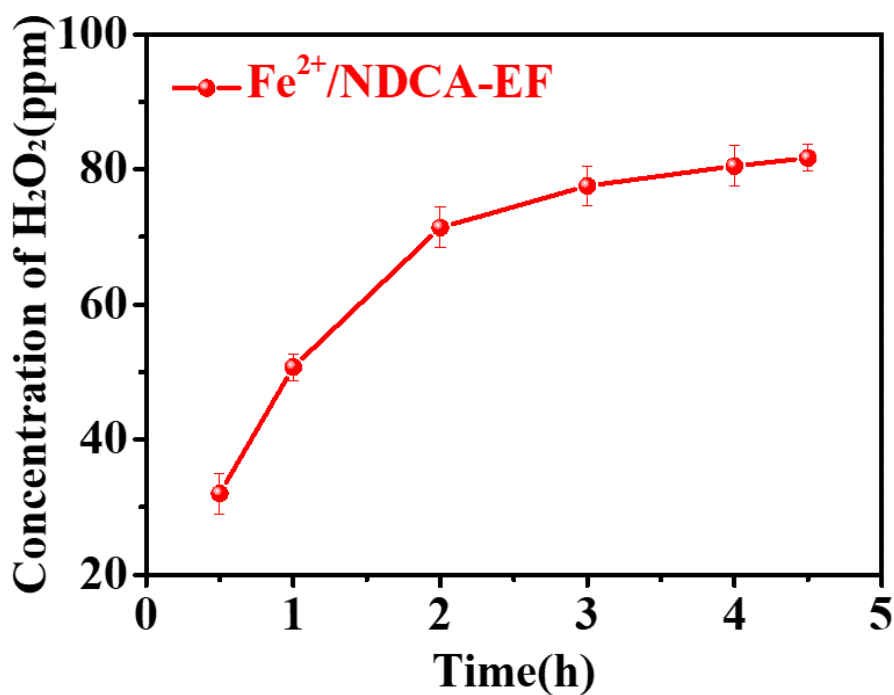


Figure S9. The ability of NDCA cathode for continuously producing H₂O₂ in EF system with constant current of 20 mA (3.33 mA cm⁻²) during 4.5 h.

As shown in Figure S9, the concentration of H₂O₂ in EF system with NDCA cathode increased from 32.1 ± 1.2 ppm to 82.5 ± 0.7 ppm in 4.5 h. The accumulation of H₂O₂ revealed that NDCA is an efficient EF cathode that has high selectivity and activity to continuously *in-situ* produce H₂O₂.

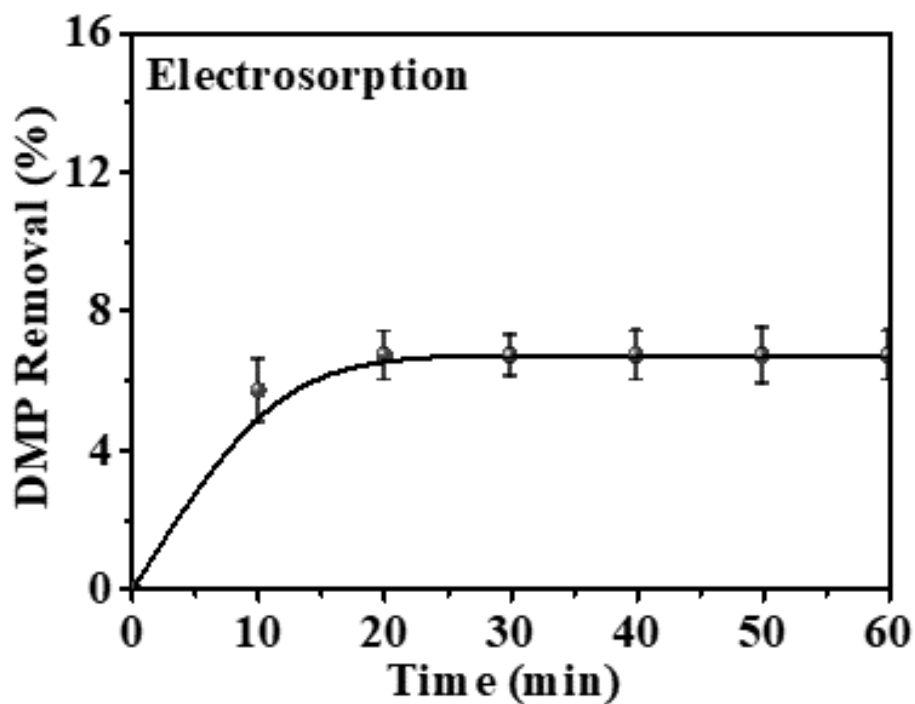


Figure S10. DMP removal efficiency in electro-sorption process with NDCA cathode.

As shown in Figure S10, the DMP removal in electro-sorption (ES) process with NDCA cathode was only $6.7 \pm 0.8\%$. The removal efficiency in ES with NDCA cathode was negligible compared with $\text{Fe}^{2+}/\text{H}_2\text{O}_2$ -EF, EO and $\text{Fe}^{2+}/\text{H}_2\text{O}_2$ -F processes.

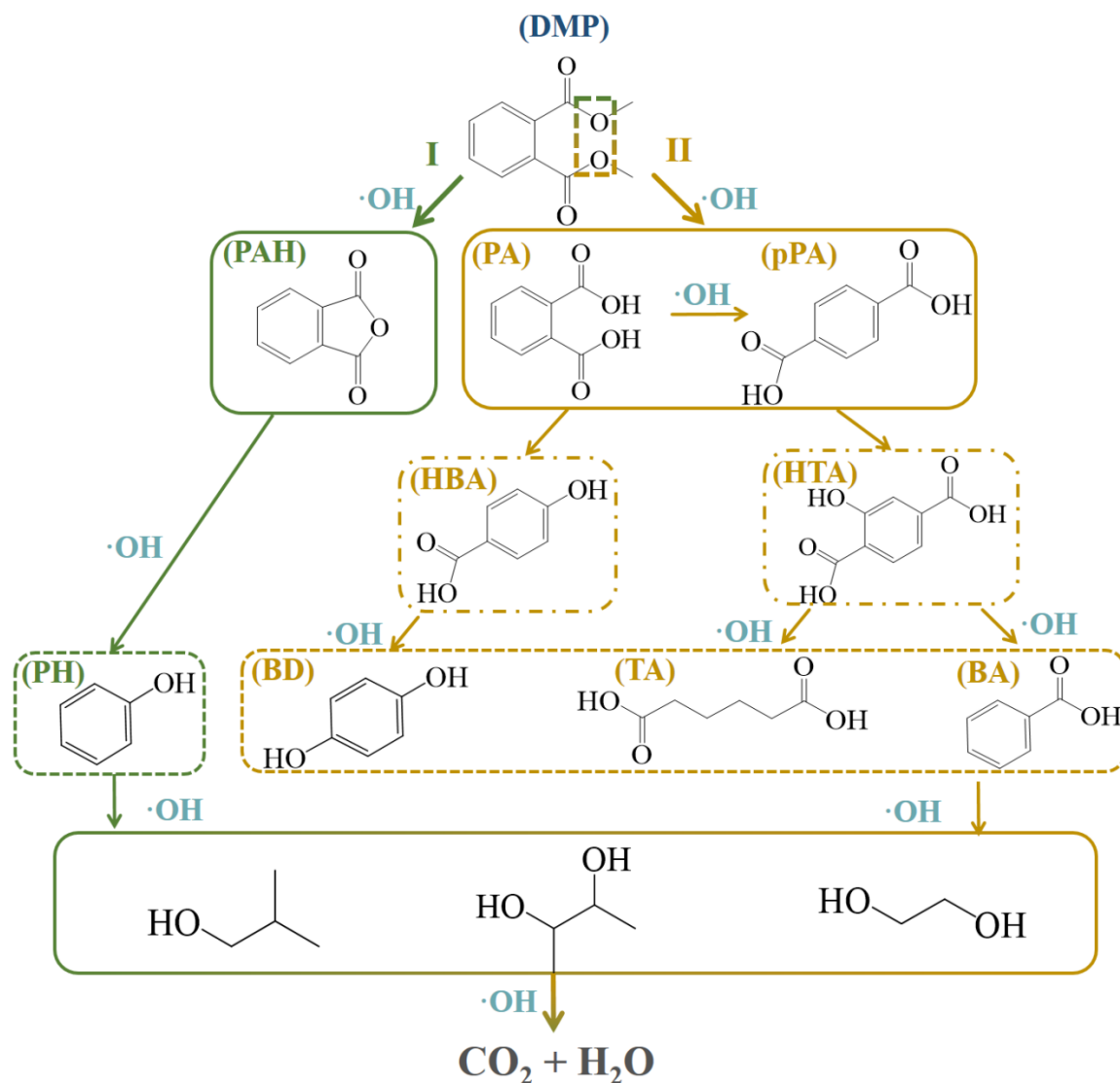


Figure S11. The degradation mechanism of DMP in $\cdot\text{OH}$ -mediated oxidation process.

The degradation of DMP by can be divided into two pathways (I and II). Firstly, the C-O bond in DMP was cleaved to form o-phthalic anhydride (PAH, route I) and phthalic acid (PA, route II). As for route I, PAH was further decarboxylated to produce phenol (PH) after being attacked by $\cdot\text{OH}$. As for route II, PA would transform into two hydroxylated intermediates including 2-hydroxyterephthalic acid (HTA) and 4-hydroxybenzoic acid (HBA). After opening the phenyl ring, HTA was decomposed as terephthalic acid (TA) and benzoic acid (BA). Simultaneously, 1,4-benzenediol (BD)

was generated after decarboxylation of HBA. Finally, all the generated intermediates including PH, TA, BA and BD were attacked by $\cdot\text{OH}$ and transformed into 2-methylpropanol, butane-2,3-diol and ethylene glycol, which was easily transformed into inorganic compounds including CO_2 and H_2O to achieve complete mineralization.

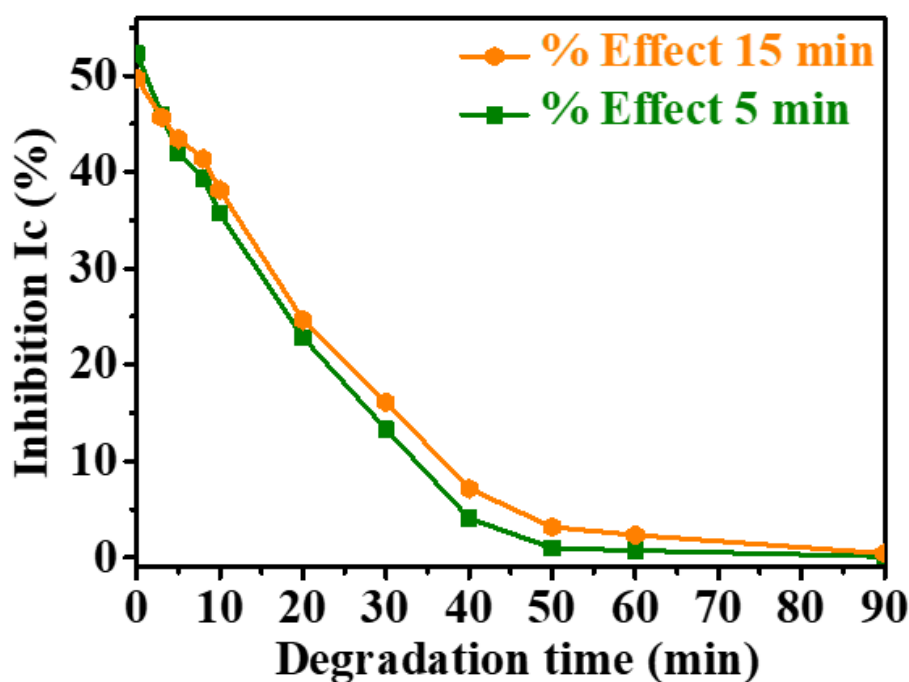


Figure S12. Evolution of the inhibition of marine bacterial luminescence after 5 and 15 min of exposure with a sample taken after different EF treatment duration for DMP degradation.

The toxicity assessments during DMP degradation in Fe^{2+} /NDCA-EF system was shown in Figure S12. The luminescence inhibition which reflects solution toxicity decreased from $50.9 \pm 1.3\%$ to $0.3 \pm 0.1\%$ after 90 min. In another word, the detoxification of the DMP solution was achieved in Fe^{2+} /NDCA-EF system. This could be linked to the formation of lower toxic intermediate products including o-phthalic anhydride (PAH), phthalic acid (PA), phenol (PH), 2-hydroxyterephthalic acid (HTA) and 4-hydroxybenzoic acid (HBA). Besides, as degradation time increased, the above intermediates will be oxidized into short-chain carboxylic acids such as terephthalic acid (TA), benzoic acid (BA), and 1,4-benzenediol (BD), which would easily transform into inorganic compounds including CO_2 and H_2O .

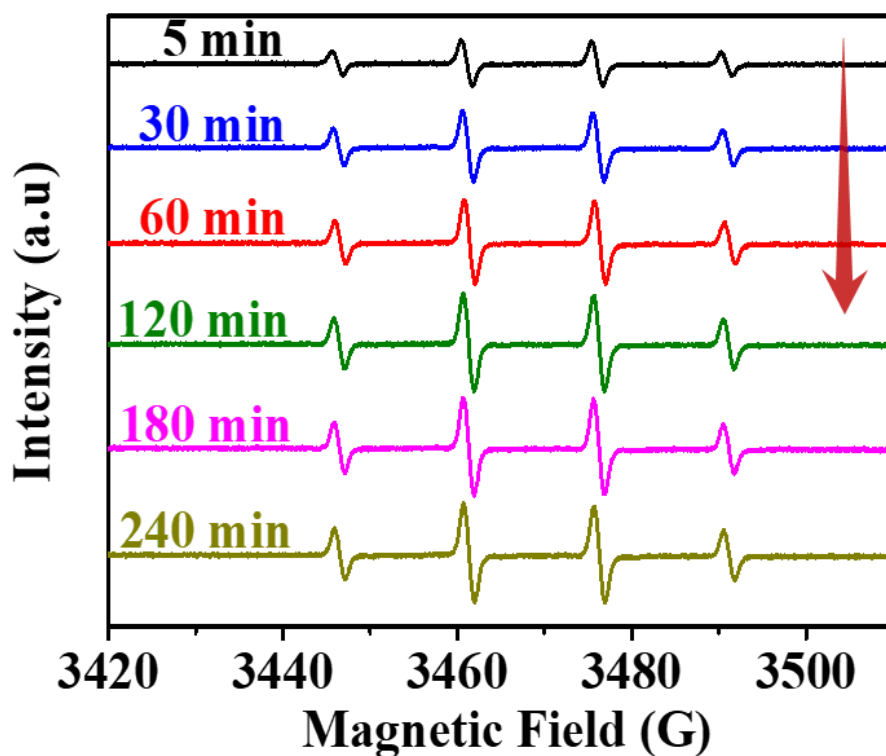


Figure S13. The ESR spectrums of Fe^{2+} /NDCA-EF system at various time of 5, 30, 60, 120, 180 and 240 min.

The ESR signal of DMPO- $\cdot\text{OH}$ adduct in Fe^{2+} /NDCA-EF system continuously increased at the first 60min and then kept at stable generation rate of $\cdot\text{OH}$ in the whole reaction process, as shown in Figure S13. The increased concentration of $\cdot\text{OH}$ is due to the enhanced accumulation of electro-generated H_2O_2 and accelerated regeneration of Fe^{2+} with NDCA cathode.

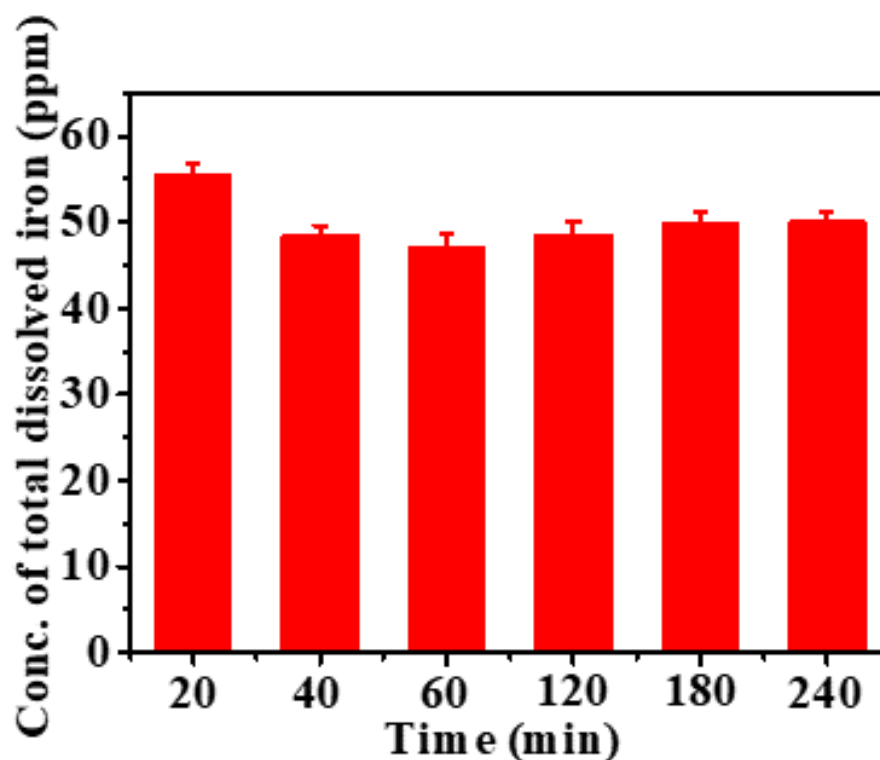


Figure S14. The concentration of total dissolved iron in Fe^{2+} /NDCA-EF system.

As shown in Figure S14, the concentration of total dissolved iron decreased from 54.9 ± 1.1 ppm to 47.2 ± 1.4 ppm in the first 60 min due to the formation of intermediate $\text{Fe}(\text{OH})_3$ sediment on NDCA cathode. Following, the amount of dissolved iron species increased to 49.7 ± 1.2 ppm at 60 min and then maintained this value within 240 min. This phenomenon resulted from the transformation of $\text{Fe}(\text{OH})_3$ sediment to soluble Fe(III) species including $\text{Fe}(\text{OH})_2^+$ and FeOH^{2+} .

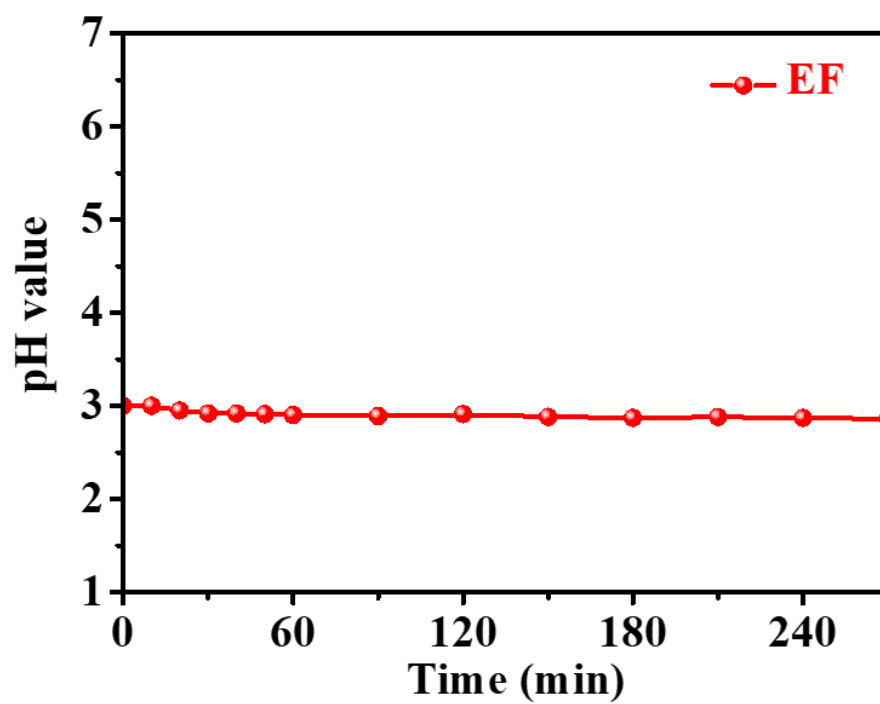


Figure S15. The pH values during the whole EF reaction from 0 to 270 min.

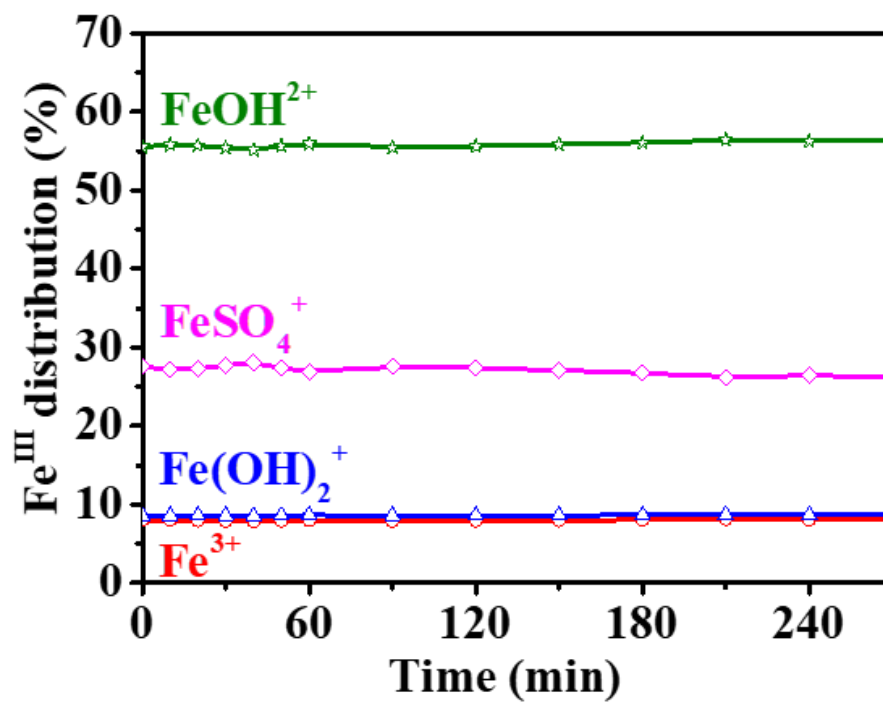


Figure S16. The Fe(III) distribution at various reaction time from 0 to 270 min.

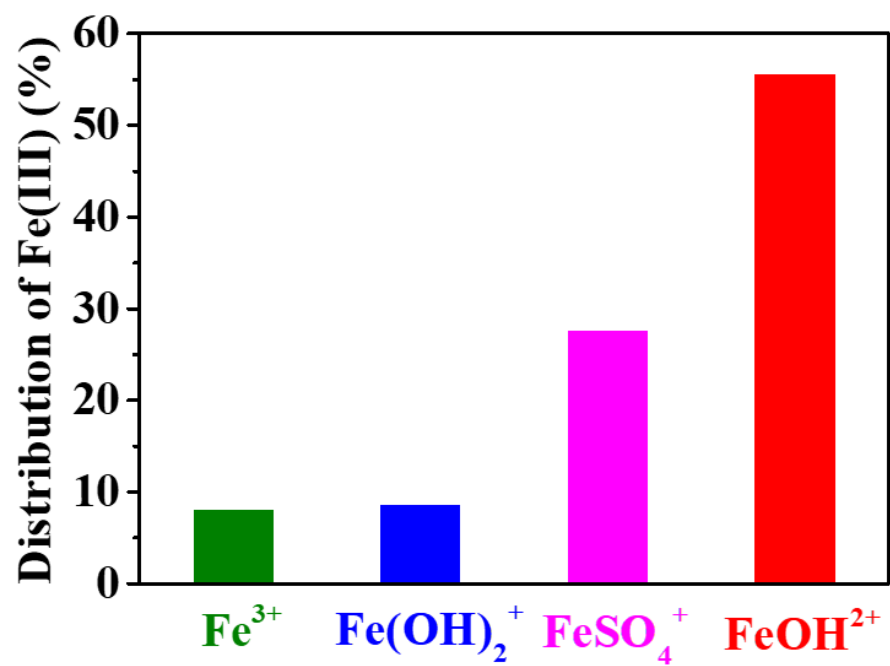


Figure S17. The distribution of Fe^{3+} , $\text{Fe}(\text{OH})_2^+$, FeSO_4^+ and FeOH^{2+} species at pH 3.

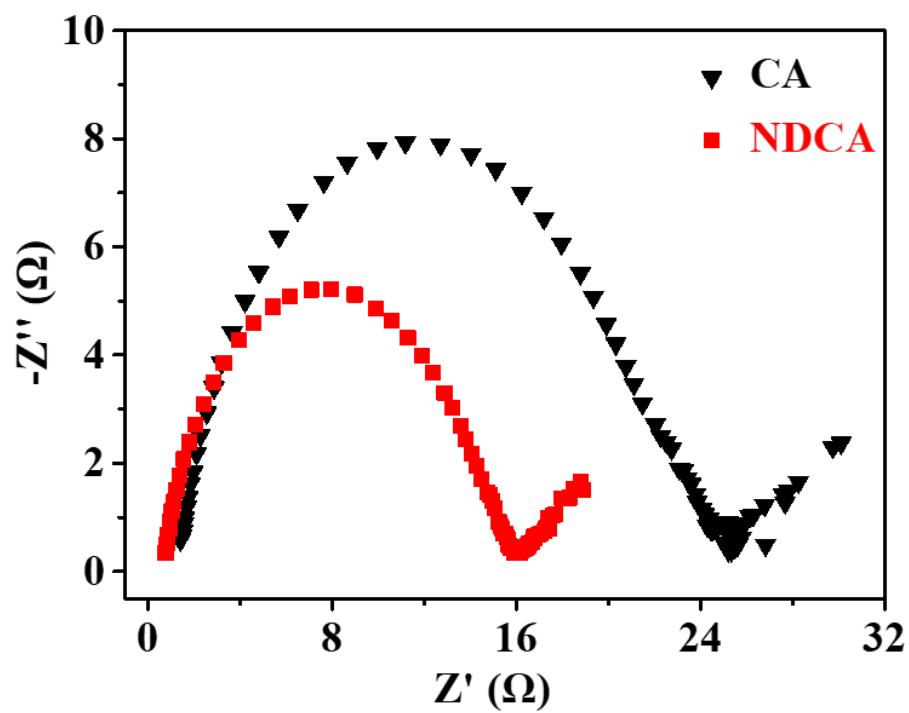


Figure S18. The Nyquist curves of CA and NDCA with the frequency from 0.1 Hz to 10000 Hz.

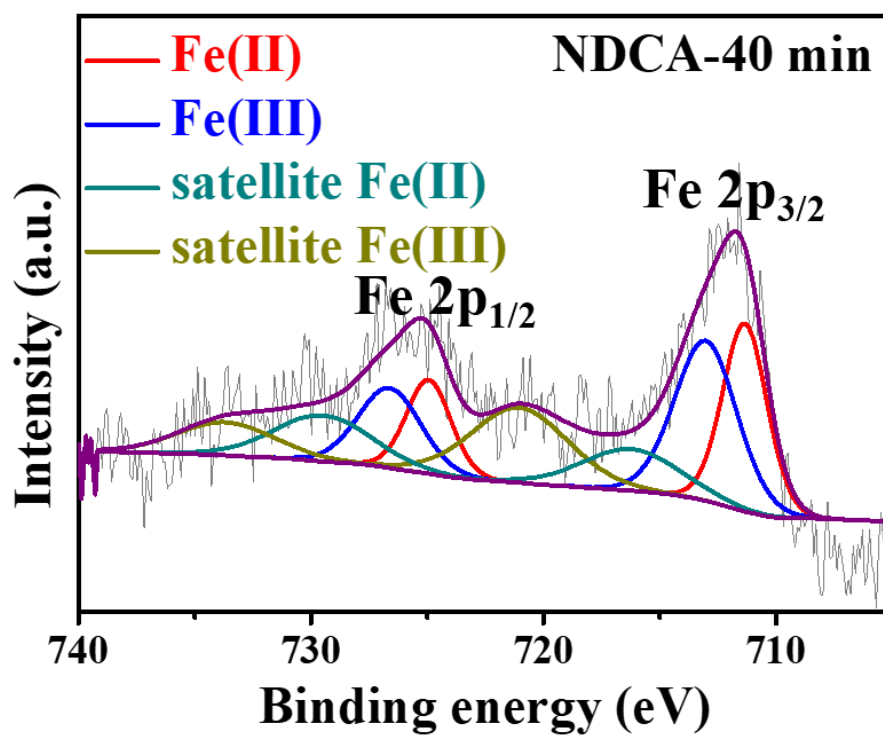


Figure S19. The Fe 2p spectrum of NDCA cathode after EF reaction for 40 min.

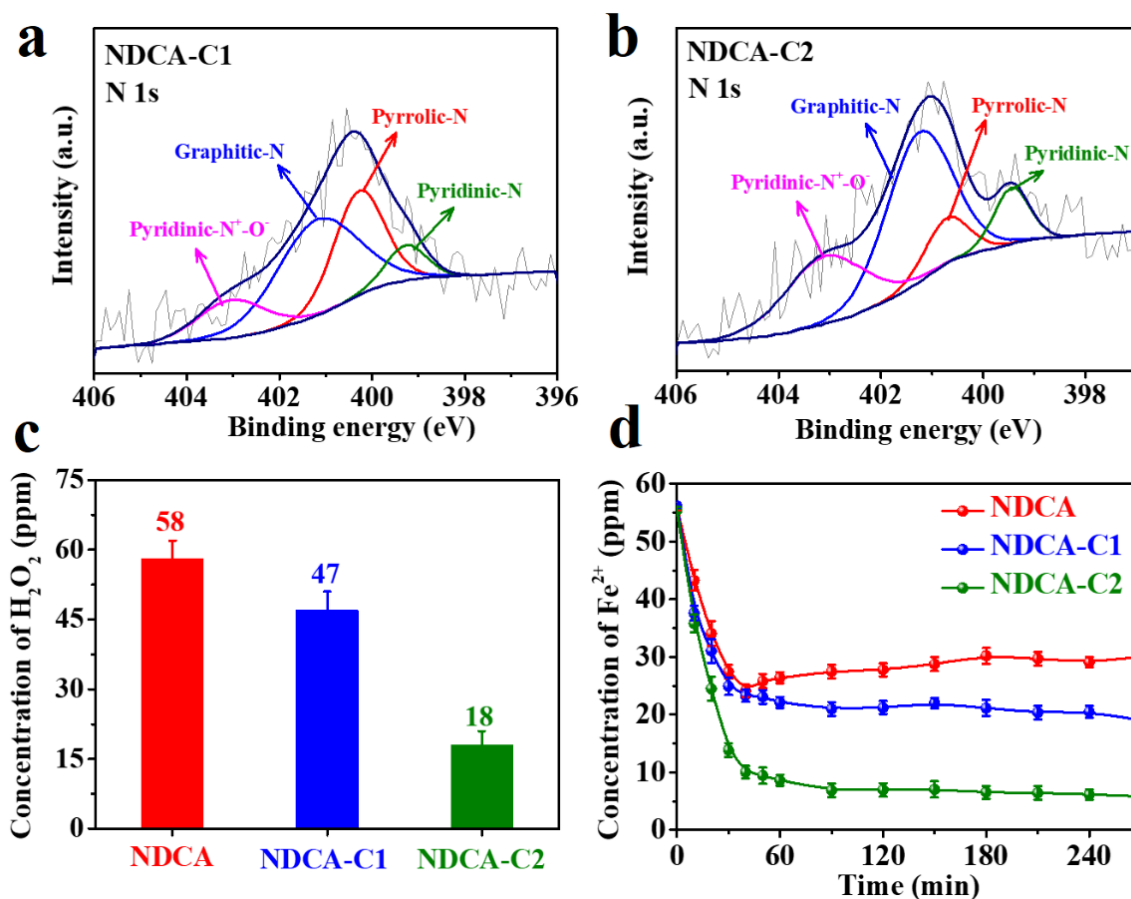


Figure S20. The N 1s spectrum of (a) NDCA-C1 and (b) NDCA-C2. (c) H₂O₂ yield by NDCA, NDCA-C1 and NDCA-C2 after 60 min with current of 20 mA. (d) The concentration of Fe²⁺ during EF reaction with same amount of 60 ppm H₂O₂ including the electro-generated H₂O₂ via cathode and externally supplied H₂O₂.

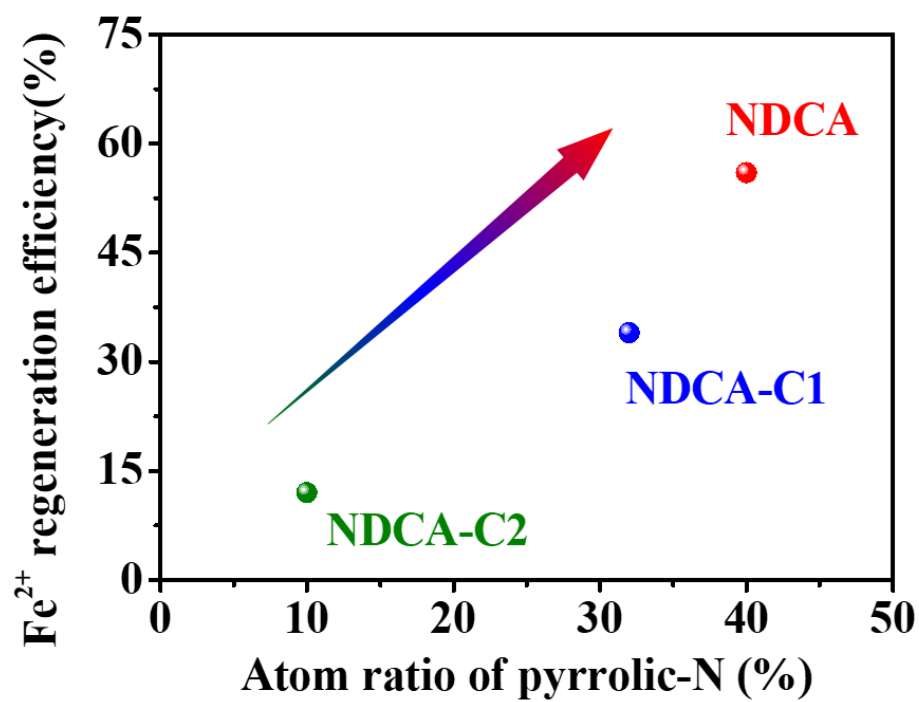


Figure S21 Fe^{2+} regeneration efficiency with different cathode including NDCA, NDCA-C1 and NDCA-C2 with different atom ratio of pyrrolic-N.

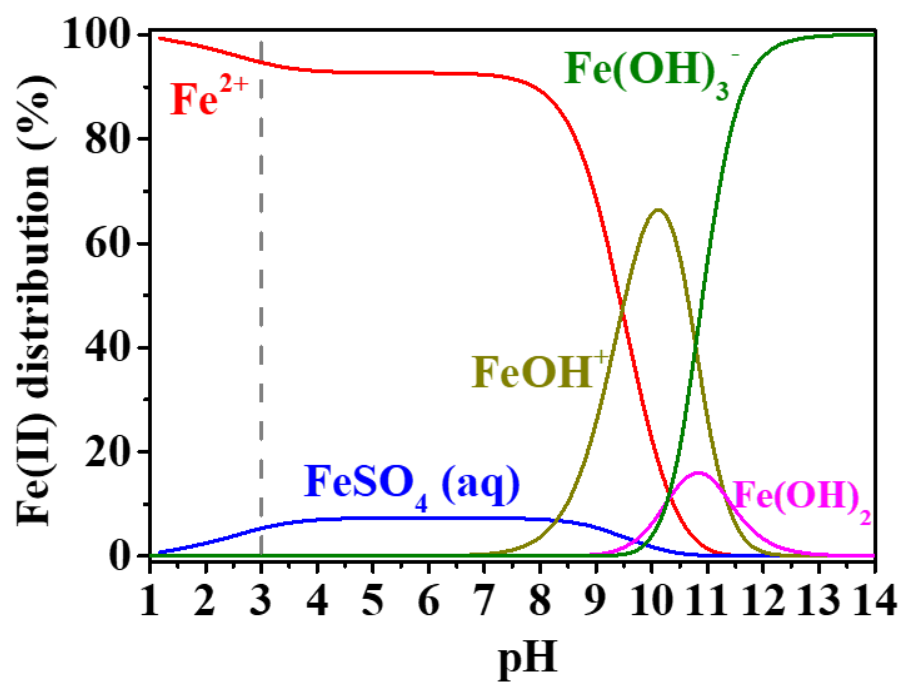


Figure S22. The Fe(II) distribution at various pH values, calculated based on the database in Visual MINTEQ.

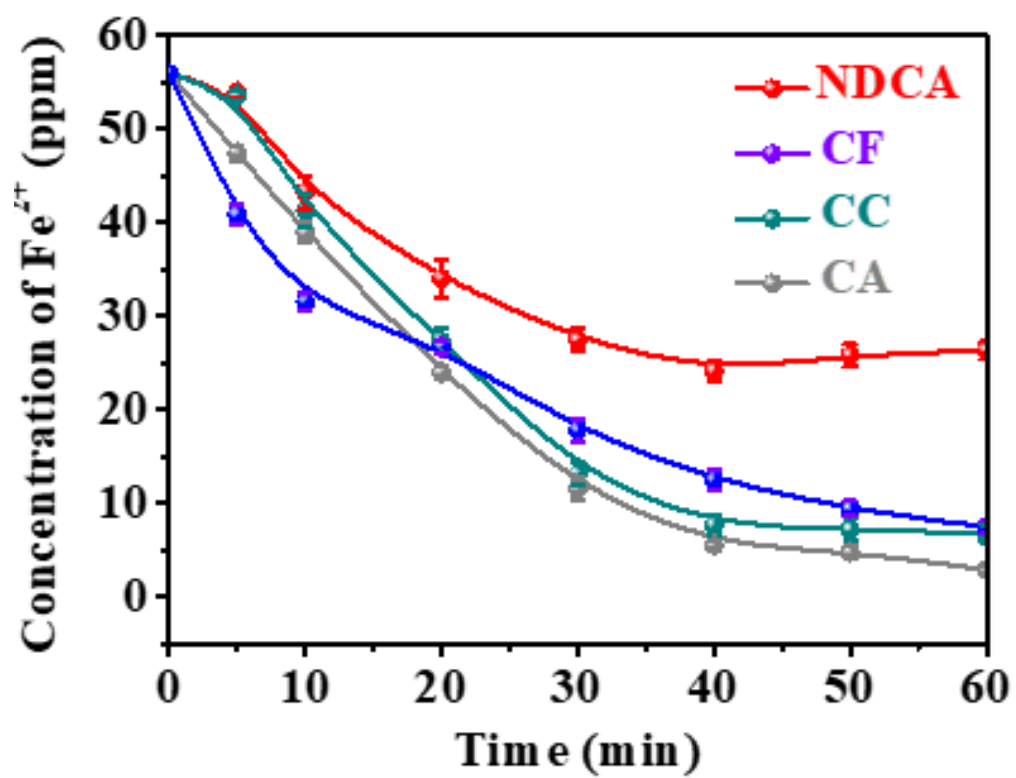


Figure S23. The concentration of Fe^{2+} in EF process with different cathodes including NDCA, CC, CF and pure CA.

REFERENCES

1. Le, T. X. H.; Nguyen, T. V.; Yacouba, Z. A.; Zoungrana, L.; Avril, F.; Petit, E.; Mendret, J.; Bonniol, V.; Bechelany, M.; Lacour, S.; Lesage, G.; Cretin, M., Toxicity removal assessments related to degradation pathways of azo dyes: Toward an optimization of Electro-Fenton treatment. *Chemosphere* **2016**, *161*, 308-318.
2. Le, T. X. H.; Nguyen, T. V.; Yacouba, Z. A.; Zoungrana, L.; Avril, F.; Nguyen, D. L., Petit, E.; Mendret, J.; Bonniol, V.; Bechelany, M.; Lacour, S.; Lesage, G.; Cretin, M., Correlation between degradation pathway and toxicity of acetaminophen and its by-products by using the electro-Fenton process in aqueous media. *Chemosphere* **2017**, *172*, 1-9.
3. He, D. Q.; Zhang, Y. J.; Pei, D. N.; Huang, G. X.; Liu, C.; Li, J.; Yu, H. Q., Degradation of benzoic acid in an advanced oxidation process: The effects of reducing agents. *J. Hazard. Mater.* **2020**, *382*, 121090.
4. Xing, M.; Xu, W.; Dong, C.; Bai, Y.; Zeng, J.; Zhou, Y.; Zhang, J.; Yin, Y., Metal Sulfides as Excellent Co-catalysts for H₂O₂ Decomposition in Advanced Oxidation Processes. *Chem.* **2018**, *4*, (6), 1359-1372.
5. Liang, J.; Zhang, Y.; Song, C.; Tang, D.; Sun, J., Double-potential electro-Fenton: A novel strategy coupling oxygen reduction reaction and Fe²⁺/Fe³⁺ recycling. *Electrochem. Commun.* **2018**, *94*, 55-58.
6. Huang, X.; Zhu, N.; Mao, F.; Ding, Y.; Zhang, S.; Liu, H.; Li, F.; Wu, P.; Dang, Z.; Ke, Y., Enhanced heterogeneous photo-Fenton catalytic degradation of tetracycline over yCeO₂/Fh composites: Performance, degradation pathways, Fe²⁺ regeneration and

mechanism. *Chem. Eng. J.* **2020**, *392*, 123636.

7. Clark, W. P.; Steinberg, S.; Dronskowski, R.; McCammon, C.; Kuppenko, I.; Bykov, M.; Dubrovinsky, L.; Akselrud, L. G.; Schwarz, U.; Niewa, R., High-Pressure NiAs-Type Modification of FeN. *Angew. Chem. Int. Ed.* **2017**, *56*, (25), 7302-7306.

8. Deng, D.; Wu, X.; Li, M.; Qian, S.; Tang, B.; Wei, S.; Zhang, J., Electrochemical degradation of three phthalate esters in synthetic wastewater by using a Ce-doped Ti/PbO₂ electrode. *Chemosphere* **2020**, *259*, 127488.

9. Li, D.; Zheng, T.; Liu, Y.; Hou, D.; He, H.; Song, H.; Zhang, J.; Tian, S.; Zhang, W.; Wang, L.; Ma, J., A cost-effective Electro-Fenton process with graphitic felt electrode aeration for degradation of dimethyl phthalate: Enhanced generation of H₂O₂ and iron recycling that simultaneously regenerates the electrode. *Chem. Eng. J.* **2020**, *394*, 125033.

10. Du, E.; Feng, X.; Guo, Y.; Peng, M.; Feng, H.; Wang, J.; Zhang, S., Dimethyl Phthalate Degradation by UV/H₂O₂: Combination of Experimental Methods and Quantum Chemical Calculation. *Clean-Soil, Air, Water* **2015**, *43*, (6), 811-821.

11. Sharma, K.; Raizada, P.; Hosseini-Bandegharai, A.; Thakur, P.; Kumar, R.; Thakur, V. K.; Nguyen, V. H.; Singh, P., Fabrication of efficient CuO/graphitic carbon nitride based heterogeneous photo-Fenton like catalyst for degradation of 2,4 dimethyl phenol. *Process Saf. Environ. Protect.* **2020**, *142*, 63-75.

12. Wang, T.; Jia, H.; Guo, X.; Xia, T.; Qu, G.; Sun, Q.; Yin, X., Evaluation of the potential of dimethyl phthalate degradation in aqueous using sodium percarbonate activated by discharge plasma. *Chem. Eng. J.* **2018**, *346*, 65-76.

13. Zhao, H.; Wang, Q.; Chen, Y.; Tian, Q.; Zhao, G., Efficient removal of dimethyl phthalate with activated iron-doped carbon aerogel through an integrated adsorption and electro-Fenton oxidation process. *Carbon* **2017**, *124*, 111-122.
14. Lan, H.; He, W.; Wang, A.; Liu, R.; Liu, H.; Qu, J.; Huang, C.P., An activated carbon fiber cathode for the degradation of glyphosate in aqueous solutions by the Electro-Fenton mode: Optimal operational conditions and the deposition of iron on cathode on electrode reusability. *Water Res.* **2016**, *105*, 575-582.